Regulation of the order–disorder phase transition in a Cs$_2$NaFeCl$_6$ double perovskite towards reversible thermochromic application

Wenzhe Li[‡, †], Naveed Ur Rahman[‡], Yeming Xian[‡], Hang Yin, Yunkai Bao, Yi Long, Songyang Yuan, Yangyi Zhang, Yaxuan Yuan, and Jiandong Fan[†]

Institute of New Energy Technology, Department of Electronic Science and Engineering, College of Information Science and Technology, Jinan University, Guangzhou 510632, China

Abstract: Multifunctional lead-free double perovskites demonstrate remarkable potential towards applications in various fields. Herein, an environmentally-friendly, low-cost, high-throughput Cs$_2$NaFeCl$_6$ single crystal with exceedingly high thermal stability is designed and grown. It obtains a cubic lattice system in the temperature range of 80–500 K, accompanied by a completely reversible chromatic variation ranging from yellow to black. Importantly, the intriguing thermochromism is proved to own extremely high reproducibility (over 1000 cycles) without a hysteretic effect, originating from its structural flexibility that including (i) the noteworthy distortion/deformation of [NaCl$_6$]$^{5-}$ and [FeCl$_6$]$^{3-}$ octahedra; (ii) order–disorder arrangement transition of [NaCl$_6$]$^{5-}$ and [FeCl$_6$]$^{3-}$ octahedra as the function of temperature. This study paves the way towards a new class of smart windows and camouflage coatings with an unprecedented colour range based on a Cs$_2$NaFeCl$_6$ perovskite.

Key words: lead-free perovskite; Cs$_2$NaFeCl$_6$ single crystal; thermochromism; crystallographic structure; order-disorder phase transition

1. Introduction

The organic–inorganic lead halide perovskites have achieved enormous development because of their outstanding optoelectronic properties[1–3], reproducible fabrication[4], compositional flexibility[5], and defect tolerance[6], among others[7]. However, it remains the debate over the intrinsically unstable crystallographic structure and the environmental impact of the lead species, which motivates efforts to find lead-free and structural stable alternatives. A promising strategy toward addressing both the toxicity and stability of the perovskite bottlenecks is to explore closely related compounds by means of designing rational perovskite materials, e.g., Cs$_2$B^{I}B^{III}X$_6$ (where B^I represents monovalent metallic cations such as Ag, Au and Cu; B^{III} represents trivalent metallic cations such as Bi, Sb and In; X = Cl, Br, I).

Recently, the Cs$_2$B^{I}B^{III}X$_6$ double perovskites continued to draw increasing attention in view of their nontoxicity and stability compared to their lead-based counterparts, which boosts their applications in various fields[8, 9]. A lead-free Cs$_2$AgInCl$_6$ perovskite was demonstrated to exhibit efficient and stable white-light emission by means of self-trapped excitons that are associated with the Jahn–Teller distortion of the [AgX$_6$]$^{5-}$ octahedron in the excited state[9]. The per-

ovskites, including both lead-free and lead halides, e.g., CH$_3$NH$_3$PbI$_{3-x}$Br$_x$[10], Cs$_2$AgBiBr$_6$[11] and (CH$_3$NH$_3$)$_4$PbI$_6$·2H$_2$O[12] perovskites, have been proved to own stable thermochromic property that enables their potential applications in the smart windows and temperature sensors. Meanwhile, Tang *et al.* employed the Cs$_2$AgBiBr$_6$ single crystals for a sensitive X-ray detector, which are allowed to obtain a detector with an extremely low detectable dose rate by means of largely eliminating Ag$^+$/Bi^{3+} disordering and improve the crystal resistivity[8]. Our recent study also found that the improved ordering extent of alternatively arranged [AgX$_6$]$^{5-}$ and [BiX$_6$]$^{3-}$ octahedra in Cs$_2$AgBiBr$_6$ structure was able to decrease the defect density and suppress self-trapped exciton formation, and thereby tune the band gap and enhance the carrier mobility[13].

However, there remains largely undeveloped alternatives for such a class of lead-free double-perovskites. Rational designing of emerging perovskite material and its based optoelectronic devices will be significantly boosted by means of understanding the structure–property relation in the lead-free double halogen perovskite system[14, 15], e.g., the order–disorder regulation and its potential dynamic mechanism of [B^{I}X$_6$]$^{5-}$/[B^{III}X$_6$]$^{3-}$ octahedra arrangement.

In this study, we design and grow a lead-free double Cs$_2$NaFeCl$_6$ perovskite single crystal with highly thermal stability. Compared to the Cs$_2$AgBiBr$_6$ double perovskite, the Cs$_2$NaFeCl$_6$ obtains a wider band gap, and we extend the temperature range for thermochromism to a low-temperature region. The as-grown single crystal exhibits fantastic thermochromic behaviour in the temperature range of 80–500 K. The poten-

Wenzhe Li, Naveed Ur Rahman, and Yeming Xian contributed equally to this work.
Correspondence to: W Z Li, li_wz16@jnu.edu.cn; J D Fan, jdfan@jnu.edu.cn

Fig. 1. (Color online) Colour evolution of as-prepared $Cs_2NaFeCl_6$ single crystal as the function of temperature in the range of 80–500 K.

2. Experimental

2.1. Cs₂NaFeCl₆ single crystal growth

The $Cs_2NaFeCl_6$ perovskite single crystals were prepared by the method of temperature cooling crystallization. Particularly, 0.4040 g cesium chloride (CsCl, 99.99%, Aladdin), 0.050 g sodium chloride (NaCl, 99.9%, Aladdin) and 0.1920 g iron(III) chloride hexahydrate ($FeCl_3 \cdot 6H_2O$, 99%, Acros) were mixed with 9 mL of hydrochloric acid (HCl, 36 wt%–38 wt%, STREAM POWER). The solution was heated on the hot plate under the temperature of 140 °C for 5 h for complete dissolution. Then the temperature was decreased by the rate of 1 °C/h from 140 to 120 °C. Finally, the solution was cooled down from 120 to 20 °C by the rate of 0.5 °C/h. The orange $Cs_2NaFeCl_6$ single crystals formed at the bottom of the glass vessels.

2.2. Electronic structure calculations

We employed the Real Space Electronic Structure CalcUlator (RESCU) and a density functional theory (DFT) calculation package to simulate the electronic structures of the $Cs_2NaFeCl_6$ double perovskite under different ambient temperature of 200, 300 and 400 K, respectively, which was based on the linear combination of atomic orbitals (LCAO) basis set. In the self-consistent calculation, the general gradient approximation of Perdew–Burke–Ernzerhof (GGA-PBE) exchange correlation functional was selected to define the exchange correlation energy in the Kohn–Sham equation. A $4 \times 4 \times 4$ Monkhorst–Pack special k mesh grid method was used to integrate the Brillouin zone. The convergence criteria for the self-consistent calculation were set to 1×10^{-5} e and 1×10^{-5} eV for the charge density and total energy, respectively, and the 0.3 Bohr real space resolution was set. We have not considered the spin–orbit coupling (SOC) effect in the calculation since the negligible influence of SOC on the $Cs_2NaFeCl_6$ perovskite without a heavy atom.

2.3. Characterizations

$Cs_2NaFeCl_6$ perovskite single crystals were crushed and ground to fine powder, then characterized by a Bruker D8 Advance X-ray diffractometer (XRD) with Cu Kα radiation at 40 kV and 40 mA. The step and the time are set to be 0.01° and 0.2 s, respectively. The single crystal powder was sandwiched between glasses, and the glass on one side was at-

tached with a heating ring. A temperature controller and liquid nitrogen pump were provided by Oxford Instruments. The UV−vis spectra measurement of the single crystals was carried out by placing a single crystal in a double-beam spectrophotometer equipped with an integrating sphere (Cary 5000, Agilent Technologies). X-ray photoelectron spectroscopy (XPS) spectra were measured with Thermo K-Alpha+. XPS spectra were shifted to account for sample charging using inorganic carbon at 284.80 eV as a reference. The $Cs_2NaFeCl_6$ perovskite single crystals are mounted on an XtaLAB PRO CCD area-detector diffractometer, equipped with a graphite monochromator situated in the incident beam, for data collection at a temperature in the range of 80–400 K. The determination of unit-cell parameters and data collection were performed using the scan technique with Mo Kα radiation. The single-crystal structure was resolved and refined by SHELXT and OLEX2[16−18]. The TGA and DSC analysis were obtained on a STA 449 F5 analyzer from room temperature to 800 °C at a rate of 10 °C/min in a flowing nitrogen atmosphere. Specific-heat was measured by the differential scanning calorimetry method using a simultaneous thermal analyser (NETZSCH DSC 404C). The $Cs_2NaFeCl_6$ was ground to powder and then pressed into pallet with the size of ϕ 10 × 2 mm³ for the measurement of thermal diffusion coefficient, it was measured by the laser flash method using a laser flash apparatus (NETZSCH LFA 447 Nanoflash) over the temperature range from 300 to 420 K.

3. Results and discussion

The $Cs_2NaFeCl_6$ single crystal was prepared via the self-crystallization method in a saturated precursor solution by means of slowly decreasing the solution temperature. Details can be found in the experimental section. The $Cs_2NaFeCl_6$ single crystal with a regular octahedron can be grown up to 6 mm in length by governing the growth time and precursor concentration (Fig. S1(a)), by which its exposure surfaces were dominated by the {111} plane family. Note that its morphology can be controlled via carefully tuning the temperature field and regulating the growth rate of exposure surfaces, e.g., (−111), (1−11) and (11−1) planes as shown in the schematic representation of the stereographic projection (Figs. S1(b) and S1(c)), which enables us to obtain various morphologies that likely trigger some potential applications (Figs. S1(d)–S1(f)). X-ray photoelectron spectroscopy (XPS) characterizations certify the composition of as-prepared $Cs_2NaFeCl_6$ single crystal without any impurity (Fig. S2).
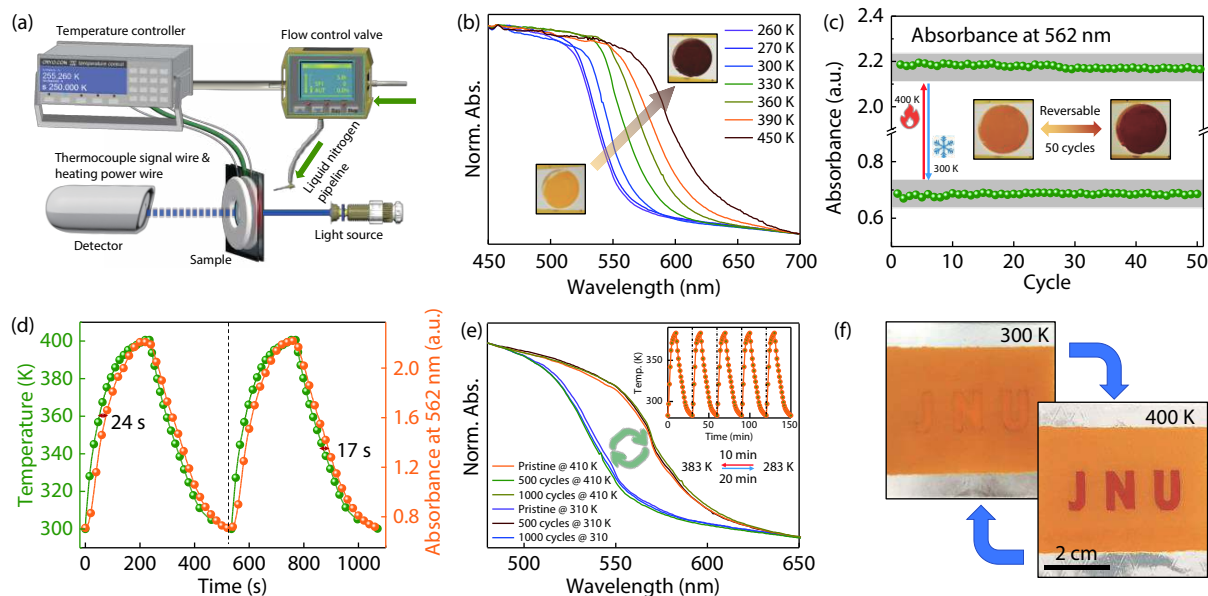
We explored the changes of the morphology and optical

Fig. 2. (Color online) (a) Schematic view of in-situ characterization system of UV–vis spectrum. (b) UV–vis spectra of the $Cs_2NaFeCl_6$ single crystal pallet as the function of temperature from 260 to 450 K. (c) The stable and reversible switching of the absorption (562 nm) of the $Cs_2NaFeCl_6$ single crystal pellet over 50 cycles. (d) Temperature variation of the perovskite single crystal in the range of 300–400 K during the heating-cooling process (green line), the orange line is the corresponding absorbance intensity of the $Cs_2NaFeCl_6$ single crystal pellet at 562 nm as the function of temperature. (e) Absorbance curves of $Cs_2NaFeCl_6$ single crystal pellet at 310 and 410 K after 500 and 1000 cycles, respectively. Inset shows the corresponding temperature variation procedure within 5 cycles. (f) Photograph of the prototype device with patterned "JNU" at the cold state (300 K) and hot state (400 K) for perovskite smart displaying.

properties of the $Cs_2NaFeCl_6$ single crystal under different temperatures (Fig. 1). Interestingly, we detected an obvious thermochromic phenomenon of the $Cs_2NaFeCl_6$ perovskites for both powder and a single crystal under transitional temperatures. Particularly, with increasing temperature from 80 to 500 K, the colour of the $Cs_2NaFeCl_6$ single crystal varied from light yellow to dark red. Remarkably, its colour was able to completely recover to their original colour with refrigeration treatment from 500 to 80 K, which suggests that the thermochromic behaviour of the $Cs_2NaFeCl_6$ single crystal is utterly reversible. Such a characteristic enables the application of $Cs_2NaFeCl_6$-based smart windows, and using the photosensitive sensor to regulate the temperature of the windows is considered to be an effective method to control the color variation of the windows.
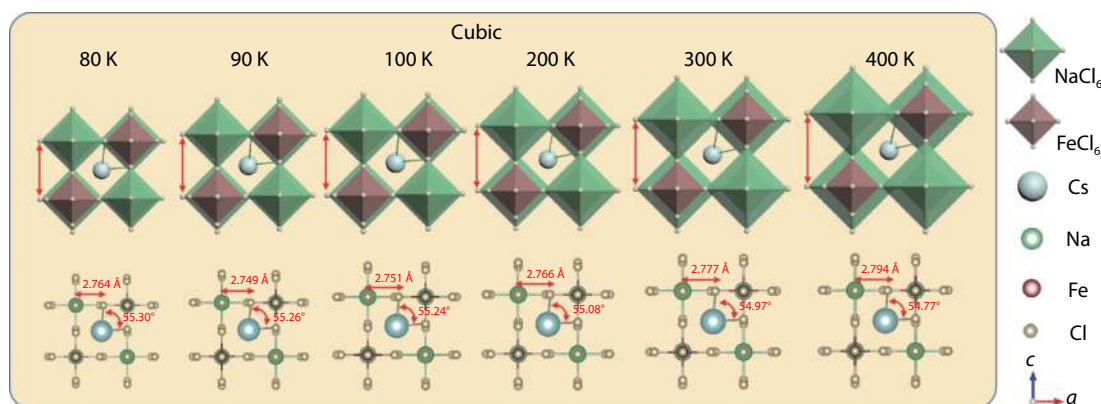
The gradual darkening of the crystal colour suggests a narrowed process of its band gap. The *in-situ* ultraviolet–visible (UV–vis) absorption spectra as the function of temperature was performed by means of heating/cooling cycles of the $Cs_2NaFeCl_6$ perovskite powders (Fig. 2(a)). As expected, its absorption edges exhibit observable shift (579–660 nm) towards the infrared region upon increasing the sample temperature from 260 to 450 K, which is in accordance to the colour change of $Cs_2NaFeCl_6$ single crystal (Fig. 2(b)). Through extrapolating the linear region of the absorption edge to the energy-axis intercept, we can obtain the optical band gaps with the values in the range of 1.88–2.14 eV (Fig. S3). Likewise, we measured the absorbance ability when fixing the wavelength at 562 nm upon different temperature (300 and 400 K) with the aim of checking its reversibility (Fig. 2(c)). After 50 cycles, it remains extremely stable thermochromic behaviour without hysteretic effect, i.e., the absorbance curves are overlapped with temperature cycles, which further verifies that

the chromatic variation is reversible and reproducible. In order to certify whether the absorbance peak position can entirely recover to its original position, i.e., the hysteresis effect, we performed the *in-situ* absorbance characterizations by means of repeating the heating and cooling cycle as the function of treatment time. Clearly, the thermochromic behaviour is closely in accordance to the temperature variation (Fig. 2(d)), which is superior to that of the 3D $MAPbI_3$ perovskite with an observable delay that was related to the local inclusions of each phase[19]. Remarkably, the absorbance curves of the $Cs_2NaFeCl_6$ single crystal pellet demonstrates nearly the same after 500 and 1000 cycles, respectively, demonstrating extremely high reproducibility and stability (Fig. 2(e)). We fabricated a prototype device with a printed "JNU" pattern, by which it displayed homogeneous yellow throughout the glass at 300 K, whereas the patterned "JNU" was localized displaying at 400 K that was printed by the $Cs_2NaFeCl_6$ single crystal ink (Fig. 2(f) and video in the supporting information).

With the aim of studying the temperature-induced discoloration process and the corresponding thermal dynamics of the as-prepared $Cs_2NaFeCl_6$ perovskite single crystal, we carried out the thermogravimetric analysis (TGA) characterization and the results are shown in Fig. S4(a). It is clearly observed that the $Cs_2NaFeCl_6$ crystal structure starts to decompose when the temperature rises to ~662 K, which far exceeds the widely used lead based organic–inorganic hybrid perovskites[20, 21]. Likewise, the curve of differential scanning calorimeter (DSC) measurement of $Cs_2NaFeCl_6$ perovskites displays a closed and reversible loop (Fig. S4(b)). The crystal system transition-induced endothermic and/or exothermic peaks was not observed, which discloses that no transition of the crystal system occurs in this regard. The TGA/DSC plots cer-

Table 1.   Crystallographic parameters of the as-prepared $Cs_2NaFeCl_6$ single crystals at different temperatures.

Crystal type	$Cs_2NaFeCl_6$ (80 K)	$Cs_2NaFeCl_6$ (90 K)	$Cs_2NaFeCl_6$ (100 K)	$Cs_2NaFeCl_6$ (200 K)	$Cs_2NaFeCl_6$ (300 K)	$Cs_2NaFeCl_6$ (400 K)
CCDC NO.	2041648	2041647	2001471	2001470	2001473	2001472
Formula weight	1114.72 g/mol	1114.72 g/mol	1114.72 g/mol	1114.72 g/mol	1114.72 g/mol	1114.72 g/mol
Crystal system	Cubic	Cubic	Cubic	Cubic	Cubic	Cubic
Space group	Fm-3m	Fm-3m	Fm-3m	Fm-3m	Fm-3m	Fm-3m
Unit-celldimensions	$a = b = c =$ 10.2591(2) Å, $\alpha = \beta = \gamma = 90°$	$a = b = c =$ 10.26506(14) Å, $\alpha = \beta = \gamma = 90°$	$a = b = c =$ 10.2679(2) Å, $\alpha = \beta = \gamma = 90°$	$a = b = c =$ 10.3028(5) Å, $\alpha = \beta = \gamma = 90°$	$a = b = c =$ 10.3270(6) Å, $\alpha = \beta = \gamma = 90°$	$a = b = c =$ 10.3622(4) Å, $\alpha = \beta = \gamma = 90°$
Volume	1079.76(6) Å³	1081.64(4) Å³	1082.54(6) Å³	1093.62(16) Å³	1101.35(19) Å³	1112.64(14) Å³
Z	2	2	2	2	2	2
Radiation	Mokα (λ = 0.71073)	Mokα (λ = 0.71073)	Mokα (λ = 0.71073)	Mokα (λ = 0.71073)	Mokα (λ = 0.71073)	Mokα (λ = 0.71073)
Reflections collected	3115	3065	305	316	207	298
Final R indexes [all data]	$R_1 = 0.0113$, $wR_2 = 0.0281$	$R_1 = 0.0125$, $wR_2 = 0.0343$	$R_1 = 0.0129$, $wR_2 = 0.0308$	$R_1 = 0.0179$, $wR_2 = 0.0424$	$R_1 = 0.0207$, $wR_2 = 0.0471$	$R_1 = 0.0336$, $wR_2 = 0.0584$
Goodness-of-fit on F2	1.277	1.302	1.186	1.127	1.121	0.999
Largest difference map peak/hole	0.234/–0.472e Å⁻³	0.342/–0.572e Å⁻³	0.34/–0.61e Å⁻³	0.37/–0.88e Å⁻³	0.42/–0.60e Å⁻³	0.62/–0.52e Å⁻³

Fig. 3. (Color online) Crystal structures of as-prepared $Cs_2NaFeCl_6$ single crystal at different temperature. Wyckoff positions of B-site atoms: Fe01 (1,1/2, 1/2, 4a), Na01 (1/2, 1/2, 1/2, 4b).

tify that the as-prepared $Cs_2NaFeCl_6$ perovskite single crystals are thermally stable, which further rules out the likelihood of the transition of the crystal system as a factor of thermochromism. The stability performance of phase and energetics of $Cs_2NaFeCl_6$ perovskite in the range of 200–500 K would be likely in accordance to its gradual lattice expansion. The corresponding density was also calculated as the function of temperature (Fig. S4(c)).

Fig. S4(d) displays the specific heat of $Cs_2NaFeCl_6$ perovskite as the function of the temperature, which was carried out by the method of differential scanning calorimetry. Clearly, the specific heat of the $Cs_2NaFeCl_6$ crystal is almost linear with a value of 0.60–0.63 J·g⁻¹·K⁻¹ in the temperature range of 283–425 K. Accordingly, the corresponding molar specific heat of the crystal is various from 334.42 to 351.14 J·K⁻¹, the relatively higher specific heat suggests that the temperature fluctuation is smaller inside the lattice structure during the endothermal and/or endothermic process of the $Cs_2NaFeCl_6$ perovskite-based thermochromic device.

Fig. S4(e) illustrates the thermal diffusion coefficients of the $Cs_2NaFeCl_6$ crystal pallet in the temperature range from 300 to 420 K at 30 K intervals between measured temperature points. Its thermal conductivity can be calculated with

the measured specific heat and thermal diffusion coefficient following the equation:

$$K = \lambda \rho C_p, \tag{1}$$

where K, λ, ρ and C_p denote respectively the principal thermal conductivity, thermal diffusion coefficient, density and specific heat of the $Cs_2NaFeCl_6$ crystal. Correspondingly, the calculated thermal-conductivity components of the $Cs_2NaFeCl_6$ are 0.92 W·m⁻¹·K⁻¹ at 300 K and 0.75 W·m⁻¹·K⁻¹ at 420 K (Fig. S4(f)), which are inversely proportional to the temperature and comparably to the widely used laser crystals[22].

As discussed above, the variation in temperature would result in a colour deepening/lightening of the $Cs_2NaFeCl_6$ single crystal, which is likely associated with the structural transformation[23]. In order to profoundly explore the crystallographic structure and phase transition of the $Cs_2NaFeCl_6$ perovskite, we recorded the *in-situ* variable-temperature X-ray diffraction data from the exactly the same $Cs_2NaFeCl_6$ perovskite single crystal at different temperature (80, 90, 100, 200, 300, 400 K) *via* liquid nitrogen controlling, and the corresponding single crystal structures were resolved and refined by SHELXT and OLEX2[16–18]. The corresponding crystallograph-

ic parameters are presented in Table 1 and Tables S1–S7 and CIF files in the supporting information, and the stochiometric view of the corresponding 3D structure evolution of $Cs_2NaFeCl_6$ single crystal at different temperature are also provided in Fig. 3. Structurally, the $Cs_2NaFeCl_6$ single crystal exhibited a traditional double-perovskite structure with the space group of Fm-3m, where the $[NaCl_6]^{5-}$ and $[FeCl_6]^{3-}$ octahedra share the halide atoms at the corner to form a 3D structure with high symmetry alongside the temperature variation in range of 80–400 K (Fig. 3 and Table 1). The structure phase (Fm-3m) is exactly the same as the traditional lead-free double perovskites, e.g., $Cs_2AgBiBr_6$[13], $Cs_2AgInCl_6$[9], in which the rock-salt ordering of B-site cations are energetically arranged, predominantly owing to the large discrepancy of charge between trivalent and monovalent B-site cations. Herein, the overall bond lengths and thereby the unit cell along b-axis inside the perovskite lattice structure display linearly increasing as the function of increased temperature (Fig. 3 and Figs. S5(a) and S5(b)). The temperature-associated XRD patterns were carried out to explore the crystal structural variations. Fig. S6 displays the diffraction peaks that tend to shift towards lower diffraction angles upon increasing temperature. Particularly, the (022) plane at 24.5° shifts to 24.3°, whereas the (004) plane at 34.9° moves to 34.5°. Such a shift is associated with the lattice expansion process of the lattice structure. Again, the peaks gradually shift back toward higher diffraction angles during the cooling process, signifying a reversible process as observed in colour change. The structural evolution of the $Cs_2NaFeCl_6$ single crystal is capable of quantitative representation of the reversable thermochromism by means of the lattice spacing parameter d at each temperature. Again, the corresponding diffraction intensity, FWHM and calculated unit cell are proved to be temperature-dependent and reversible without hysteresis (Fig. S7).

Considering the varieties of the bond length in the $Cs_2NaFeCl_6$ structure with respect to the octahedron distortion, the bond relaxation function for the perovskite structure can be written as follows[24]:

$$\eta(x) = \frac{R_{Na-Cl}(x) - R_{Fe-Cl}(x)}{R^0_{Na-Cl} - R^0_{Fe-Cl}}, \qquad (2)$$

where $R_{Na-Cl}(x)$ and $R_{Fe-Cl}(x)$ are the nearest-neighbour bond lengths in an $Cs_2NaFeCl_6$ structure with highly ordering extent of $[FeCl_6]^{3-}$ and $[NaCl_6]^{5-}$ octahedra, and $R^0_{Na-Cl}(x)$ and $R^0_{Fe-Cl}(x)$ are the previous-neighbour-bond lengths in the $Cs_2NaFeCl_6$ structure with relatively lower distortion. In the temperature range of 80–400 K, the bond lengths of Fe–Cl and Na–Cl display linearly enlarged tendency as the function of increasing temperature (Table S1 and Fig. S5(b)), which thereby gives rise to enlarged $[NaCl_6]^{5-}$ and $[FeCl_6]^{3-}$ octahedra (Fig. 3). It was previously reported that similar thermochromic phenomenon was induced by the variation of the Sb–Br interatomic distances within analogous $[SbBr_6]^{4-}$ octahedron[25]. Herein, during the increasing temperature process, a geometric distortion is typically observed among $[NaCl_6]^{5-}$ and $[FeCl_6]^{3-}$ octahedra where the bond length of Na–Cl and Fe–Cl can be longer than their previous counterparts. The corresponding $\eta(x)$ is calculated to be 1.12 by using the crystallographic parameters (Table S1). Such relaxation obviously affects the double perovskite formation enthal-

pies through the appropriate deformation potentials. The discrepancy of expansion extent between them would give rise to the octahedra distortion, which would inevitably result in an expected distortion of cubic lattice structure (Fig. 3 and Fig. S5). In view of the bond angles of Cl–Cs–Cl (Na) and Cl–Cs–Cl (Fe) (Fig. S5(c)), we propose the distortion would structurally regulate the band gap of $Cs_2NaFeCl_6$ perovskites as well as its colour, which we will elucidate afterward in combination with the in-situ structural characterizations and theoretical calculation results.

The order–disorder transition of octahedra arrangement in the double perovskite lattice structure was recently evidenced to be capable of affecting the absorbance band edge and accordingly the crystal colour[9, 13]. The B-site cations, i.e., Fe^{3+} and Na^+, occupy the following Wyckoff positions: 4a (0, 0.5, 0.5) and/or 4b (0.5, 0.5, 0.5), respectively. A large discrepancy between the B-cations in perovskite lattice would strongly drive the structure towards ordering arrangement by electric forces. In sublattice structure of rock-salt-ordered double perovskites, the B-sited cations associated antisites are deep acceptors and will be the dominant defects[26]. In this concern, both the direct Na–Fe exchange and the vacancy assisted exchange, e.g., Fe_{Na} and Na_{Fe} antisites, likely dominate the order–disorder transition.

The order–disorder transition follows the Vineyard's theory of order–disorder kinetics as the function of temperature[27]:

$$\frac{dS}{dt} = \frac{1}{2}\left[K_O(1-S)^2 - K_D(1+S)^2\right], \qquad (3)$$

where $S = 1$ for a perfectly ordered perovskite, K_O and K_D are the rate constants for ordering and disordering, respectively. In the case of fcc structure, K_O and K_D are presented as follows:

$$\frac{K_O}{K_D} = 12f \cdot \exp\left(\frac{-U \pm 3\upsilon S}{K_B T}\right), \qquad (4)$$

where f and U are the frequency of the vibrational mode and activation energy associated with direct interchange of two neighbouring atoms, respectively. Besides, $\upsilon = (V_{AA} + V_{BB} - 2V_{AB})/2$, where V_{AA}, V_{BB} and V_{AB} represent the pairwise interaction effective energy between nearest neighbours AA, BB and AB (Consider a pair composed of an A atom on site r and a B atom on a neighbouring site r + δ). When the environmental temperature is altered, the lattice structure tends to reach a new equilibrium, while the order–disorder transition kinetics exponentially depend on the temperature[28].

The corresponding value of S in "Ord-$Cs_2NaFeCl_6$" can be calculated by means of assessing the experimental value of I_{111}/I_{220}, i.e., the diffraction intensity ratio of the (111) and (220) planes according to the extinction law in the crystal structure (Fig. 4(a)). It is generally accredited that a lower ratio embodies the inferior ordering extent in such a class of the double perovskite structure, i.e., the presence of more antisite defects of Fe^{3+} and Na^+, vice versa[29]. Herein, the ordering extent parameter (S_{OEP}) for the $Cs_2NaFeCl_6$ single crystal can be quantitatively determined via calculating the intensity ratio of the observed reflection to the base lattice reflection for the single crystal with ideal ordering extent as formulated in the following[30]:
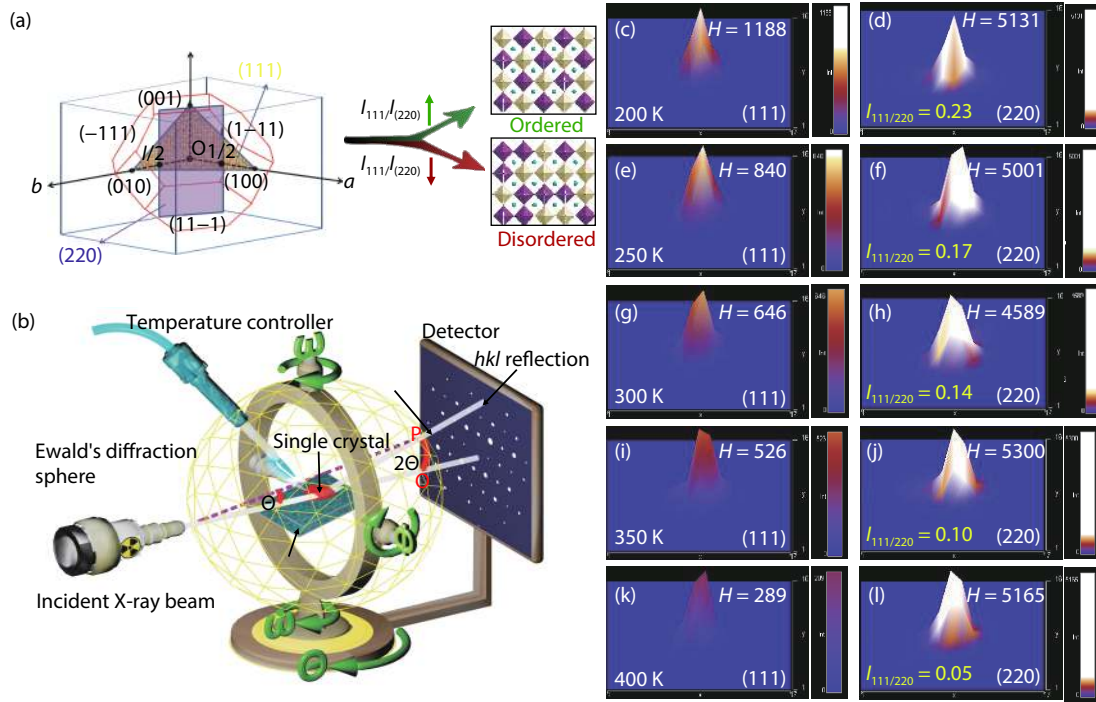
Fig. 4. (Color online) (a) Schematic view of the planes in face centred cubic (fcc) crystal and the order-disorder phase transition. (b) Schematic view of in-situ characterization system of diffraction planes. (c–l) Diffraction intensity evolution of Cs$_2$NaFeCl$_6$ single crystal in reciprocal space as the function of temperature.

$$S_{OEP} = \left(\frac{I_{111}}{I_{220}}\right)_{observed} / \left(\frac{I_{111}}{I_{220}}\right)_{calc.}, \qquad (5)$$

where $S = 1$ for a perfectly ordered perovskite with superlattice structure and $S = 0$ for a fully disordered perovskite with a sublattice structure. In particular, the diffraction planes in a reciprocal space of the Cs$_2$NaFeCl$_6$ single crystal were *in-situ* characterized upon different temperature (Fig. 4(b)). With the temperature increasing, the ratio value of $(I_{111}/I_{220})_{observed}$ tends to be smaller, which decreases from 0.23 to 0.05 that is calculated from the intensity ratio of corresponding diffraction planes in the reciprocal space (Figs. 4(c)–4(l)). The ratio value of $(I_{111}/I_{220})_{calc.}$ was obtained from XRD patterns calculated from the resolved single crystal structure with ideal ordering extent. The S_{OEP} value was accordingly calculated to decrease from 0.67 to 0.28 as the temperature increases, which experimentally certifies that the ordering extent of [FeCl$_6$]$^{3-}$ and [NaCl$_6$]$^{5-}$ octahedra is alleviated by means of increasing temperature (Fig. S8(a)). It should be noted that the $(I_{111}/I_{220})_{observed}$ ratio is also affected by the octahedral tilting. However, the diffraction intensity of (111) and (220) lattice planes should proportionally change with the variation of the short-range octahedral tilting extent at different temperature. Thus, the variation of I_{111}/I_{220} is mainly attributed to the order–disorder phase transition of [NaCl$_6$]$^{5-}$ and [FeCl$_6$]$^{3-}$ octahedra, and the short-range octahedral tilting makes slight contribution to the I_{111}/I_{220} variation. Importantly, the intensity ratio displays a reversible evolution, evidencing the regulable order–disorder structure transition in the Cs$_2$NaFeCl$_6$ lattice structure by means of heating and/or cooling treatment.

As discussed above, the band gap evolution is also experimentally proved to be temperature dependent (Figs. S3 and S8(b)). Evidently, both the band gap (E_g) and ordering parameter (S_{OEP}) are in agreement with the curves fitted by the Boltzmann equation ($y = y_0 + A_1(1-\exp(-x/t_1)) + A_2(1-\exp(-x/t_2))$), which is exponentially proportional to the temperature and follows the Vineyard's theory of order–disorder transition kinetics (Fig. S8). In parallel, it was theoretically proved that manipulating ordering in Cs$_2$AgBiBr$_6$ can indeed give rise to enhanced light absorption in the visible region[15]. Following this line of thought, it can be continuously regulated from the "Ord-Cs$_2$NaFeCl$_6$" with wide direct band gap to the random "Dis-Cs$_2$NaFeCl$_6$" with a small direct band gap by means of annealing/thermal treatment. A fully disordered double perovskite would alternate the lattice symmetry of the single crystal structure. To a large extent, the structure of the double perovskite with a B-site superlattice (space group Fm-3m), e.g, Cs$_2$AgBiBr$_6$, likely convert to the structure of the widely known CsPbX$_3$ perovskite with a B-site sublattice (space group Pm-3m) with respect to the order-disorder transition[31].

The temperature-dependent relationship between the structural spatial location and electronic structure of the Cs$_2$NaFeCl$_6$ perovskite can be quantificationally characterized by simulating the band structure, density of state (DOS) distribution and charge distribution of the corresponding lattice models. Fig. S9 is the calculated band structure of three Cs$_2$NaFeCl$_6$ unit cells determined at different temperature of 200, 300 and 400 K, respectively, which were obtained by employing the GGA-PBE exchange correlation functional. The letter "G" in the band diagram represents the central point of the Brillouin zone of the cubic crystal system. The result demonstrates a clear decreased tendency of bandgap values as the structure undergoes higher ambient temperature, from 0.5915 eV at 200 K to 0.5376 eV at 400 K. The direct bandgap characteristic is retained as ambient temperature changes. He-
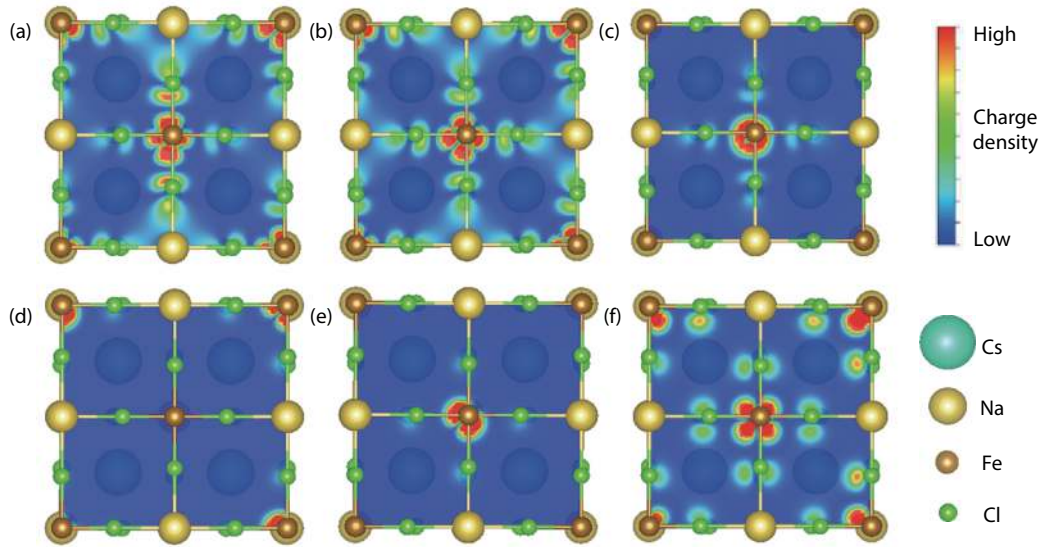
Fig. 5. (Color online) CBM and VBM-associated 2D charge density distribution maps, which are displayed on the (001) lattice plane. (a) 200 K-CBM, (b) 300 K-CBM, (c) 400 K-CBM, (d) 200 K-VBM, (e) 300 K-VBM, (f) 400 K-VBM.

rein, we attribute the temperature-dependent bandgap evolution to both interaction intensity of conductive atoms and the order–disorder phase transition in the lattice structure.

(i) Atomic interaction intensity. Fig. 5 plots the CBM-associated and VBM-associated two-dimension charge distribution along the direction of the (001) lattice plane of the $Cs_2NaFeCl_6$ perovskite at different temperatures of 200, 300 and 400 K, respectively. It is clearly observed that the VBM-associated charge distribution reaches a larger and more disperse state when the ambient temperature rises, demonstrating that the Fe–Cl interaction is strengthened compared to its counterpart at low ambient temperature. Fig. S10 displays the l-resolved projected DOS plots of the $Cs_2NaFeCl_6$ system. Obviously, near the Fermi level, the valence band maximum (VBM) is primarily derived from the Fe-3d and Cl-3p orbital states, whereas the conduction band minimum (CBM) is originated from the Fe-3d, Cl-3p and Na-3s orbital states. Since ambient temperature has a relatively small effect on orbital states of the Fe–Cl bond at CBM, the energy level of CBM can be considered stable and less temperature-dependent, while the valence band is likely broadened. The bandgap is consequently reduced in this regard.

(ii) Order–disorder phase transition. As we discussed above, the order–disorder phase may depend on the ambient temperature, in which, we assume, the existence of localized disordered phase breaks the long-period ordering of $Cs_2NaFeCl_6$ perovskite, especially on the surface. Because of the random distribution of Na and Fe, herein, we analyze the electronic structure of the randomly distributed domain by introducing the special quasirandom structures (SQSs)[32]. Under the SQS framework, the localized disorder domain can be modified as a short-period superlattice, whose structural correlation functions exhibit few discrepancies with that of infinitely/ perfectly random structure. The existence of such short-period superlattice effectively reduces the structural symmetry of $Cs_2NaFeCl_6$ perovskite, which results in the crystal-field splitting of band structure. Degenerate orbital states in the cubic $Cs_2NaFeCl_6$ structure can split in the SQS structure because the symmetry of crystal field is reduced. Thus, such a band split at the VBM leads to a broadening of electron trans-

ition energy E_0, where it can be elucidated that the individual cubic level transforms into a few SQS levels through crystal-field splitting. Such an orbital state transformation lifts the VBM and reduces E_0. Moreover, the pseudo-direct transition and inter-band mixing can largely affect the orbital state transformation between cubic $Cs_2NaFeCl_6$ structure and the corresponding SQS structure. Nevertheless, the VBM of $Cs_2NaFeCl_6$ lies in the G point, which only transforms to a single $\bar{K}$ point ($\bar{G}$ point, the bar denotes superlattice states) of the SQS structure, so the effect of pseudo-direct transition and inter-band mixing show an exceptionally insignificant influence on the cubic G state. Therefore, crystal-field splitting still plays the most important role in bandgap reduction as ambient temperature rises.

4. Conclusions

In summary, we innovatively grow a new $Cs_2NaFeCl_6$ double perovskite single crystal with an extremally high thermal stability. The as-grown $Cs_2NaFeCl_6$ perovskite single crystal is experimentally proved to own fully reversible thermochromism (over 1000 cycles) in the wide temperature range of 80–500 K, which is structurally associated with the distortion/deformation and/or rearrangement of $[NaCl_6]^{5-}$ and $[FeCl_6]^{3-}$ octahedra in a double perovskite structure. Although the pseudo-direct transition and inter-band mixing can largely affect the orbital state transformation, crystal-field splitting still plays the most important role in the order–disorder phase transition between the "Ord-$Cs_2NaFeCl_6$" and "Dis-$Cs_2NaFeCl_6$" structure, which accordingly contributes to the bandgap reduction. This study opens new perspectives toward designing novel double perovskite materials with a tuneable structure and optoelectronic properties by regulating/controlling the order–disorder arrangement of the cations at B^{3+}/B^+ sublattice, and pave the way for a new class of displaying devices, smart windows and visual thermometers based on lead-free halide double perovskites.

Appendix A. Supplementary materials

Supplementary materials to this article can be found online at https://doi.org/1674-4926/42/7/072202.

References

[1] Tsai H, Asadpour R, Blancon J C, et al. Light-induced lattice expansion leads to high-efficiency perovskite solar cells. Science, 2018, 360, 67

[2] Hu M Y, Chen M, Guo P J, et al. Sub-1.4eV bandgap inorganic perovskite solar cells with long-term stability. Nat Commun, 2020, 11, 151

[3] Shi E, Yuan B, Shiring S B, et al. Two-dimensional halide perovskite lateral epitaxial heterostructures. Nature, 2020, 580, 614

[4] Park N G, Grätzel M, Miyasaka T, et al. Towards stable and commercially available perovskite solar cells. Nat Energy, 2016, 1, 16152

[5] Saliba M, Matsui T, Domanski K, et al. Incorporation of rubidium cations into perovskite solar cells improves photovoltaic performance. Science, 2016, 354, 206

[6] Correa-Baena J P, Abate A, Saliba M, et al. The rapid evolution of highly efficient perovskite solar cells. Energy Environ Sci, 2017, 10, 710

[7] Lin J, Lai M L, Dou L T, et al. Thermochromic halide perovskite solar cells. Nat Mater, 2018, 17, 261

[8] Pan W C, Wu H D, Luo J J, et al. $Cs_2AgBiBr_6$ single-crystal X-ray detectors with a low detection limit. Nat Photonics, 2017, 11, 726

[9] Luo J J, Wang X M, Li S R, et al. Efficient and stable emission of warm-white light from lead-free halide double perovskites. Nature, 2018, 563, 541

[10] Zhang Y, Tso C Y, Iñigo J S, et al. Perovskite thermochromic smart window: Advanced optical properties and low transition temperature. Appl Energy, 2019, 254, 113690

[11] Ning W H, Zhao X G, Klarbring J, et al. Thermochromic lead-free halide double perovskites. Adv Funct Mater, 2019, 29, 1807375

[12] Halder A, Choudhury D, Ghosh S, et al. Exploring thermochromic behavior of hydrated hybrid perovskites in solar cells. J Phys Chem Lett, 2015, 6, 3180

[13] Yuan W N, Niu G D, Xian Y M, et al. In situ regulating the order-disorder phase transition in $Cs_2AgBiBr_6$ single crystal toward the application in an X-ray detector. Adv Funct Mater, 2019, 29, 1900234

[14] Esser B, Hauser A, Williams R, et al. Quantitative STEM imaging of order-disorder phenomena in double perovskite thin films. Phys Rev Lett, 2016, 117, 176101

[15] Yang J X, Zhang P, Wei S H. Band structure engineering of $Cs_2AgBiBr_6$ perovskite through order-disordered transition: A first-principle study. J Phys Chem Lett, 2018, 9, 31

[16] Sheldrick G. SHELXL-97: crystal structure refinement program. University of Göttingen, Germany Göttingen, 1997

[17] Sheldrick G. SHELXTL, structure determination software suite. Version 6.14, Bruker AXS, Madison Google Scholar, 2000

[18] Dolomanov O V, Bourhis L J, Gildea R J, et al. OLEX2: a complete structure solution, refinement and analysis program. J Appl Crystallogr, 2009, 42, 339

[19] Osherov A, Hutter E M, Galkowski K, et al. The impact of phase retention on the structural and optoelectronic properties of metal halide perovskites. Adv Mater, 2016, 28, 10757

[20] Han Q F, Bae S H, Sun P Y, et al. Single crystal formamidinium lead iodide ($FAPbI_3$): Insight into the structural, optical, and electrical properties. Adv Mater, 2016, 28, 2253

[21] Baikie T, Fang Y N, Kadro J M, et al. Synthesis and crystal chemistry of the hybrid perovskite (CH_3NH_3)PbI_3 for solid-state sensitised solar cell applications. J Mater Chem A, 2013, 1, 5628

[22] Fan J D, Zhang H J, Wang J Y, et al. Growth and thermal properties of $SrWO_4$ single crystal. J Appl Phys, 2006, 100, 063513

[23] Li L N, Sun Z H, Ji C M, et al. Rational design and syntheses of molecular phase transition crystal materials. Cryst Growth Des, 2016, 16, 6685

[24] Zunger A, Wei S H, Ferreira L G, et al. Special quasirandom structures. Phys Rev Lett, 1990, 65, 353

[25] Zhang W C, Sun Z H, Zhang J, et al. Thermochromism to tune the optical bandgap of a lead-free perovskite-type hybrid semiconductor for efficiently enhancing photocurrent generation. J Mater Chem C, 2017, 5, 9967

[26] Xiao Z W, Meng W W, Wang J B, et al. Thermodynamic stability and defect chemistry of bismuth-based lead-free double perovskites. ChemSusChem, 2016, 9, 2628

[27] Vineyard G H. Theory of order-disorder kinetics. Phys Rev, 1956, 102, 981

[28] Rey G, Redinger A, Sendler J, et al. The band gap of $Cu_2ZnSnSe_4$: Effect of order-disorder. Appl Phys Lett, 2014, 105, 112106

[29] Lim T W, Kim S D, Sung K D, et al. Insights into cationic ordering in Re-based double perovskite oxides. Sci Rep, 2016, 6, 19746

[30] Setter N, Cross L E. The contribution of structural disorder to diffuse phase transitions in ferroelectrics. J Mater Sci, 1980, 15, 2478

[31] Yin H, Xian Y M, Zhang Y L, et al. Structurally stabilizing and environment friendly triggers: Double-metallic lead-free perovskites. Sol RRL, 2019, 3, 1900148

[32] Wei S H, Ferreira L G, Bernard J E, et al. Electronic properties of random alloys: Special quasirandom structures. Phys Rev B, 1990, 42, 9622

Wenzhe Li received his Ph.D. in the Department of Chemistry, Tsinghua University, in 2017. He joined Henry Snaith Group in Oxford University for joint cultivation in 2014–2015. Currently, he is an associate professor in Institute of New Energy Technology (iNET), College of Information Sciences and Technology at Jinan University. His current research focuses on structural design of novel perovskites, optoelectronic devices, carrier transport dynamics, and device stabilities.

Naveed Ur Rahman received his Ph.D degree in 2019, as a Chinese Government Scholarship student from Sun Yat-sen University. Afterward, he joined as a post-doctoral researcher in New Energy Materials Institute, Jinan University. Presently, he is working on the improvement of the intrinsic and extrinsic stability of perovskite solar cells through structure analysis of perovskite materials.

Yeming Xian received his bachelor's degree in the Department of Electronic Engineering, Jinan University, in 2020. He joined Jiandong Fan and Wenzhe Li research group in Institute of New Energy Technology (INET), Jinan University in 2017-2020. He will start his graduate research in 2021 and his current research interests lie on First-principles calculations, optoelectronic devices and carrier behaviors in novel perovskites.

Jiandong Fan obtained his Ph.D. from the University of Barcelona in 2013. Afterward, he worked in Swinburne University of Technology and Oxford University as a postdoc. Currently, he is a full professor in Institute of New Energy Technology (iNET), College of Information Sciences and Technology at Jinan University. His research interests include crystallographic characterizations, and thin-film photoelectric and photovoltaic devices.